Research Article | Vol. 10, No. 2 | 1 Feb 2019 | BIOMEDICAL OPTICS EXPRESS 961
Biomedical Optics EXPRESS

Diffuse reflectance spectroscopy-enhanced drill for bone boundary detection

MATTHIEU DUPERRON,[1,3,*] AND KONSTANTIN GRYGORYEV,[1,3,4] GERARD NUNAN,[2] CORMAC EASON [1], RAY BURKE,[1] KEVIN MANLEY,[2] JACQUELINE GUNTHER,[1] AND PETER O'BRIEN[1]

[1] *Tyndall National Institute, Lee Maltings Complex, Dyke parade, Cork, Ireland, T12R5CP*
[2] *Stryker, Instruments Innovation Centre, IDA Business and Technology Park, Carrigtwohill, Cork, Ireland*
[3] *First co-authors of this publication*
[4] *konstantin.grygoryev@tyndall.ie*
[*] *matthieu.duperron@wanadoo.fr*

Abstract: Intramedullary nailing is a routine orthopedic procedure used for treating fractures of femoral or tibial shafts. A critical part of this procedure involves the drilling of pilot holes in both ends of the bone for the placement of the screws that will secure the IM rod to sections of the fractured bone. This step introduces a risk of soft tissue damage because the drill bit, if not stopped in time, can transverse the bone-tissue boundary into the overlying muscle, causing unnecessary injury and prolonging healing time due to periosteum damage. In this respect, detecting the bone-tissue boundary before break-through can reduce the risks and complications associated with intramedullary nailing. Hence, in the present study, a two-wavelength diffuse reflectance spectroscopy technique was integrated into a surgical drill to optically detect bone-tissue boundary and automatically trigger the drill to stop. Furthermore, Monte-Carlo simulations were used to estimate the maximum distance from within the bone at which the bone-tissue boundary could be detected using DRS. The simulation results estimated that the detection distance, termed the "look-ahead-distance" was ~1.5 mm for 1.3 mm source-detector fiber separation. Experimental measurements with 1.3 mm source-detector fiber separation showed that the look-ahead-distance was in the order of 250 μm in experiments with set drill rate and in the range of 1 mm in experiments where the holes were drilled by hand. Despite this difference, the automated DRS enhanced drill successfully detected the approaching bone tissue boundary when tested on samples of bovine femur and muscle tissue.

1. Introduction

Diffuse reflectance spectroscopy (DRS) technique is widely used to characterize biological tissues by quantifying spectral absorption and scattering properties. These parameters are directly related to the biomolecular composition of complex tissues such as skin [1], adipose tissue [2] or lung [3]. Direct comparison of DRS spectra can provide enough information to differentiate one type of tissue from another [4]. It has been previously shown that DRS can be used to distinguish between cancerous and healthy liver tissue [5], determine the level of cartilage degradation [6] and detect calcified lesions in breast tissue [7]. Furthermore, time-resolved DRS measurements performed on cortical bone allowed the quantification of its composition [8] as well as its mineralization [9]. Non-invasive nature of DRS as well as simple instrumentation allowed this technique to be integrated into a needle-like fiber optic probes [5, 10, 11] as well as into an orthopedic tool for real-time guidance [12]. Recent clinical studies have shown successful clinical application of DRS in transthoracic lung biopsies [13] and detection of cervical cancer [14], highlighting the capability of DRS to distinguish between tissue types. In this respect, one of the more challenging yet promising application for tissue differentiation is bone-tissue boundary detection in intricate orthopedic procedures [15]. For example, during an intramedullary (IM) nailing

#328327 https://doi.org/10.1364/BOE.10.000961
Journal © 2019 Received 13 Apr 2018; revised 28 Sep 2018; accepted 28 Sep 2018; published 30 Jan 2019

Biomedical Optics EXPRESS

procedure, the surgeon is tasked with mechanically locating two or more sections of fractured bone by inserting an intramedullary rod into the medullary cavity and securing it with interlocking screws, driven through the bone and the rod. To avoid additional mechanical strain and to ensure proper placement, pilot holes must be drilled for the screws by the surgeon. This is one of the more challenging phases because the surgeon cannot see the location of the distal and proximal holes of the IM nail and must rely on his/her experience, extensive knowledge of anatomy, 2D fluoroscopic images as well as mechanical and audio feedback from the drill. However, due to inherent variations of bone material thickness and composition between different regions of the bone as well as between patients, it is possible that the drill may cut its way into the overlying soft tissue, causing unnecessary injury, increasing recovery time as well as a risk of post-operative complications. Hence, integration of an automated bone-tissue boundary detection capability into the drilling procedure can have a positive impact on surgical outcomes, by reducing the risks outlined above [16, 17].

To date, a number of studies have been carried out in an attempt to de-risk the surgery and improve IM nailing outcomes [18–26]. These studies utilized sophisticated laser tracking and stereoscopic image overlay solutions to (1) determine the location of the proximal and distal holes of the IM nail after its insertion into the cavity [19, 22], (2) control the drilling axis after the holes were located [20, 23] and (3) control the insertion depth of a surgical tool [24–26]. These investigations showed the potential of laser guidance and 3D registration to increase the accuracy interlocking screw placement in IM nailing and the potential to control the drill depth with millimeter precision. Despite the potential to improve the surgical outcomes, the laser guidance approaches have a number of drawbacks such as complexity of the setup, associated cost, heavy reliance on fluoroscopic or harmful X-Ray imaging and depth control accurate to a millimeter, which is insufficient when applied to smaller or thinner biological structures. The relatively low accuracy likely stems from compounding errors as the depth and position are acquired indirectly, through a number of referencing steps. In addition, extra calibration steps may be required in a clinical setting to ensure that the positioning of the tools relative to the patient is accurate, which may result in workload increase and surgery duration. Hence, implementing a more direct approach to depth measurement could improve measurement accuracy, and reduce the duration of the surgery by eliminating the additional instrument calibration procedures and the dependence on preoperative fluoroscopic or harmful X-Ray imaging. Critically, in order to improve the chances of clinical adoption, the direct depth measurement approach must be simple and without heavy dependence on additional, stand-alone equipment. Ideally, this capability should be directly integrated into the existing surgical instruments in order to maintain the established surgical procedures as much as possible. As discussed above, DRS is a good candidate to fulfill the sub-millimeter accuracy and low complexity requirements. However, previous investigations concentrated on integrating DRS into static clinical systems, designed primarily for optical measurements and assisting with diagnosis in soft tissues. Integration of DRS into a functional, rotary tool such as a drill with the aim of performing direct material thickness measurements in order to control the drilling depth with sufficient accuracy has not been attempted.

Hence, to address the above challenge, a two-wavelength DRS technique was integrated into a surgical drill with the aim of directly detecting the approaching bone-tissue boundary when drilling and using the DRS data for controlling the depth of the pilot hole. The wavelengths of 470 nm and 780 nm were selected for DRS because, in the cortical bone, their reflectance and scattering are similar. However, in blood filled soft tissue, the 470 nm is heavily absorbed by the blood compared to 780 nm resulting in a measurable differences in the power of scattered light for each wavelengths [27, 28]. This property was used to successfully discriminate between cortical bone and approaching, blood filled muscle tissue when drilling through a bovine femur sample. In this study, two layer Monte Carlo (MC) simulation using CUDAMCML code, was performed in Matlab [29]. This simulation was used to estimate the depth reached by each

Biomedical Optics EXPRESS

wavelengths in the muscle layer after the light has crossed the bone-tissue boundary. In addition to MC simulation, a surgical drill was integrated with photo diode sensors in a manner which allowed the drill to retain its full functionality. A specialized drill bit was then fitted with two plastic optical fibers (POF) for illumination and collection of light. These modifications allowed to illuminate the bone material and simultaneously collect and measure the power of scattered light when drilling. To demonstrate the advantage of this system, the real time DRS measurement was successfully used to detect and automatically stop the drill, at a distance of 0.5 to 2.5 mm from bone-tissue boundary.

The following sections will discuss the details of MC simulations, followed by description of system components and practical experiments. The final sections of the paper will discuss the experimental results and future work.

2. Materials and methods

2.1. Monte-Carlo simulations

Two layer MC simulations were performed using parallel computing, GPU based code called CUDAMCML, based on a previously developed MCML code [30]. The primary purpose for MC simulations was to estimate the penetration depth of 470 nm and 780 nm wavelengths into the blood filled muscle tissue after traversing the bone with thickness of 5≥ d≥ 0 mm (Fig. 1).

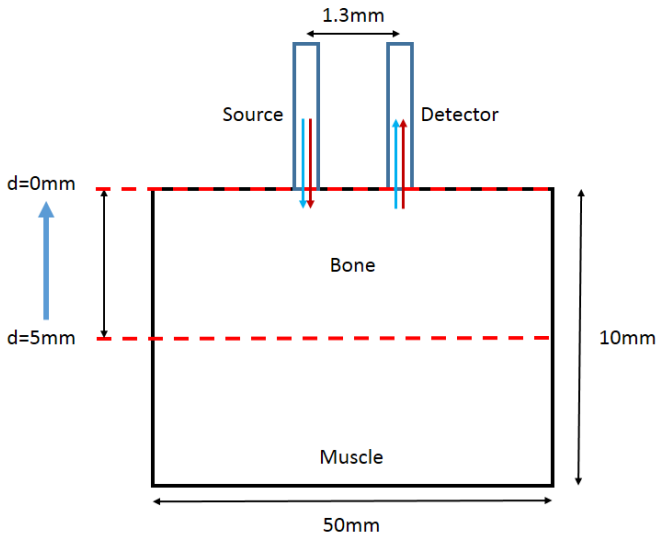

Fig. 1. Schematic of scattering layer and fiber configuration used in Monte-Carlo simulation. The source-detector distance of 1.3 mm was matched to distance between the POF fibers, integrated into experimental drill bits. The simulation was performed for a range of bone thickness values, ranging from the maximum of 5 mm down to a minimum of 0 mm (thick blue arrow).

The MC model consisted of one source and one detector fiber 500 μm in diameter coupling light in and out of a two layers of scattering media (bone and muscle). The distance between source and detector was set to 1.3 mm to match the inter-fiber distance of POFs integrated into the drill bit. The optical properties used in the simulation were previously described in [9,31,32] and listed in Table 1. In the simulation, $g = 0.9$ and 1×10^6 photon packages were injected from the source fiber.

Biomedical Optics EXPRESS

Table 1. Table of optical properties for blood [31] and bone [9, 32] used in MC simulation.

Wavelengths	Muscle			Bone		
	$\mu_a\ (mm^{-1})$	$\mu_s\ (mm^{-1})$	n	$\mu_a\ (mm^{-1})$	$\mu_s\ (mm^{-1})$	n
470 nm	8	400	1.42	0.15	36	1.6
780 nm	0.4	250	1.39	0.03	30	1.6

2.2. DRS implementation in a surgical drill

In order to perform DRS measurement in real time when drilling through bone, a modified version of surgical hand drill (CD4, Stryker, USA) was used. The three most critical challenges were: i) illumination of bone at the cutting site, ii) collection of reflected diffuse light and iii) measurement of power of collected light. Figure 2 presents the schematics and mechanical relationships of the critical components.

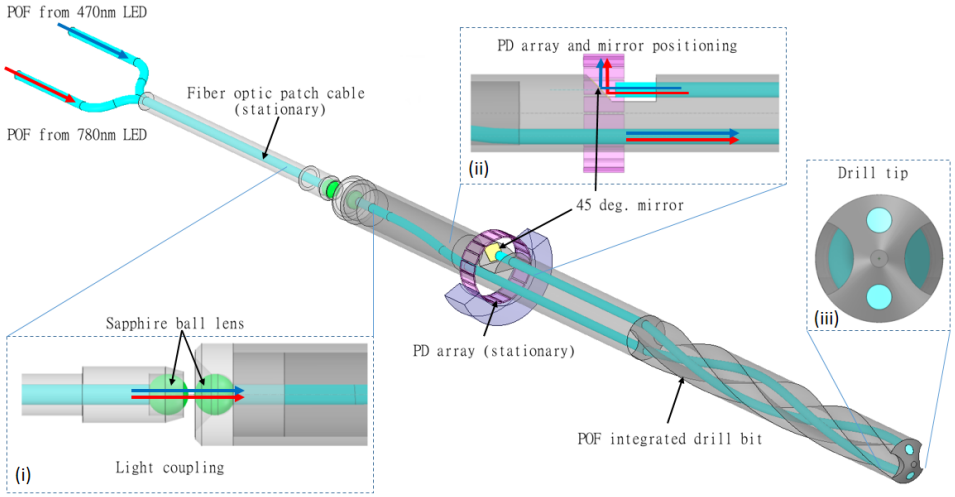

Fig. 2. Schematics of fiber integrated drill bit and the optical patch cable. Inset (i) shows how the light is coupled between a stationary LED pair through the optical patch cable into a rotating drill bit using a pair of ball lenses at the ends of each component. Inset (ii) shows the light from the LEDs being guided to the drill tip (iii) via a POF (bottom). The diffuse light is then collected by a second POF (top) on the drill tip and patched to the 45° mirror. The mirror, in turn, reflects the collected diffuse light at an array of PDs which convert the light intensity into electrical current of corresponding magnitude.

The illumination of the cut surface was performed using 470 nm and 780 nm fiber coupled LEDs (M470F3 and M780F2, Thorlabs, UK). The light from the LEDs passed through two optical stages: i) the fiber optic patch cable and ii) the drill bit. The purpose of the fiber optic patch cable was to couple the light from the stationary LEDs into a rotating drill bit as shown in Fig. 2. The patch cable was fabricated using three sections of POFs (500 μm diameter, NA 0.51,

Biomedical Optics EXPRESS

Edmund Optics, UK), a 2 mm sapphire ball lens (Edmund Optics, UK) and a custom machined cylindrical holder. Two POF section were each bonded to two SMA905 connectors (ThorLabs, UK), the free ends of these sections were then patched into a single POF which in turn was secured inside the cylindrical holder and bonded to a ball lens using UV adhesive (Norland 68, Norland, USA). The cylindrical holder was sized to fit the coolant port at the back of the CD4 hand drill and allowed secure attachment of the optical patch cable to the instrument.

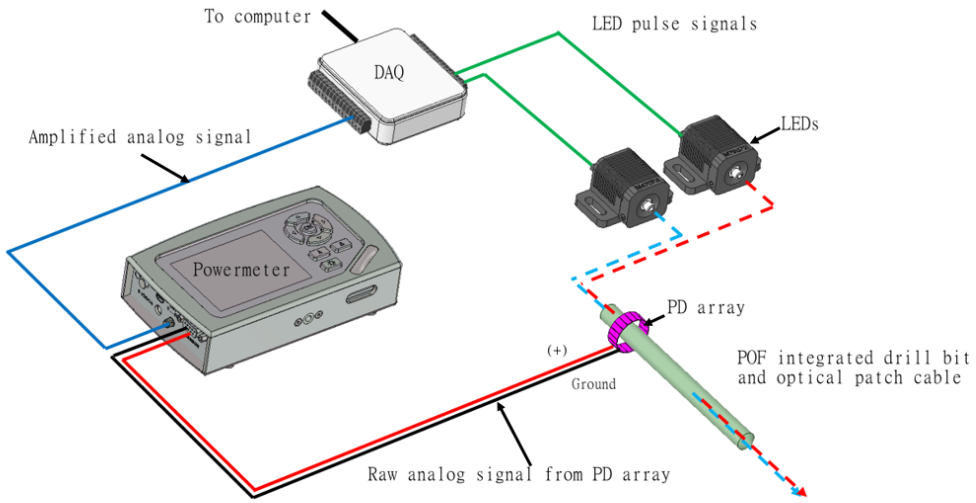

Fig. 3. Schematics of data acquisition components. the analog signal from the PD array (black and red trace) was first amplified using the PM100 power meter. The amplified signal from the power meter (blue solid trace) was then routed to an analog input channel of the DAQ for digital conversion. Additionally, the DAQ was also used to pulse the LEDs via two analog output channels (green traces).

Two POFs of the same specification as used in the patch cable, were integrated into coolant channels of a surgical drill bit. A 2 mm sapphire ball lens was attached to the back end of the drill bit using UV adhesive. The purpose of the ball lens was to collect the light from a stationary fiber optic patch cable and guide it into one POF inside the drill bit (Fig. 2(i)). This POF was termed the "source" fiber. The second POF inside the drill bit, termed the "detector" fiber, was coupled to a mirror, positioned within the drill bit at 45° relative to longitudinal axis (Fig. 2(ii)). Both, source and collector fibers, terminated on the opposing relief surfaces of the drill tip cutting geometry (Fig. 2(iii)). The mirror reflected the collected light from the fiber onto an array of silicon photo diodes (S-4V, OSI Optoelectronics, USA), integrated into the chuck of the drill. The photo diodes (PD) were positioned radially, around the portion of the drill bit with the mirror. This positioning allowed the light power measurements to be performed during the entire 360° rotation of the drill bit. The current output from the photo diodes was proportional to the power of incident light. All the PDs in the array shared a common output and ground and were connected to a single analog input channel on the Thorlabs PM100 power meter. The power meter amplified the signal from all of the PDs (Fig. 3). The amplified signal was then digitized using NI DAQ (USB-6003, National Instruments, USA).

In order to perform the DRS measurements for each wavelength, the 470 nm and 780 nm LEDs were pulsed 180° out of phase at 180 Hz and 50% duty cycle such that only one light source was

Biomedical Optics EXPRESS

on at a time for a period of 11.1 msec each. The DAQ sampling rate was 360 Hz, which is 2X LED pulse rate. The start of data acquisition and LED pulses were hardware synchronized and both were triggered when a 5 V pulse was received by PIO and PIF inputs of the DAQ. Using this method, the odd and even numbered data points, stored as 2D array on the computer, were synchronized with 470 nm and 780 nm LEDs, respectively. The array was then indexed and split into odd and even numbered datasets. The odd numbered data set was divided by the even numbered dataset to produce the optical power ratio. Following the ratio calculation, a 100 msec integration was applied to the ratio to further reduce noise and fluctuations.

The measurements were also referenced to the point in time when the drill tip cut through the bone-tissue interface. This referencing was achieved by performing each drilling experiment on a load cell which showed a steep drop in load as the drill bit exited hard bone into soft tissue. The drilling experiments were divided into two groups. In the first group, the rate of the cut (motion of drill bit through any structure of the sample) was set to 1 mm sec^{-1}. This was achieved by mounting the drill onto a mobile gantry on a vertical frame. The gantry motion and speed were controlled via a linear motor and LabView. This setup removed the variation of force and drill feed rate that exist when drilling by hand. The second group involved drilling the bone while holding the drill in hand and modulating the force and drill speed by "feel" and mechanical feedback as a surgeon would. Unless stated otherwise, the measurements were performed through the entire cross section of the bone, drilling through cortical bone, marrow, cortical bone again and finally through the muscle tissue.

2.3. *Ex-vivo bovine femur preparation*

The bovine bone samples were acquired from healthy cows, directly from the local abattoir, with the muscle tissue and marrow present. The samples were stored in a fridge below 10 °C prior to performing experiments. The results presented in the following section have been gathered from separate $n = 7$ femur samples.

Biomedical Optics EXPRESS

3. Results and discussion

3.1. Monte-Carlo simulation

Figure 4 shows the photon density of 470 nm and 780 nm wavelengths at the bone-muscle interface. The simulation results indicate that both wavelengths propagate through 5 mm thick bone layer to the interface (top, left and right of Fig. 4). Importantly, it is evident that the 780 nm light propagated into muscle layer much deeper than 470 nm light, irrespective of the thickness of the bone layer. In case of 5 mm thick bone layer, the 470 nm wavelength undergoes near complete absorption, while 780 nm penetrated >~2 mm into the muscle layer. The reduction of bone layer thickness to 1 mm resulted in 470 nm propagating <1 mm into the muscle, while 780 nm propagated ~3.5 mm (middle of Fig. 4). The minimal propagation increase of the 470 nm at this distance was likely caused by the increased photon density at the interface and higher probability of photon penetration into this layer. Finally, when the bone layer was removed entirely (bottom of Fig. 4), 470 nm light underwent complete absorption, while 780 nm light still propagated ~2.5 mm into the muscle layer. These results are extremely promising and highlight the difference in behavior of 470 nm and 780 nm light in the muscle layer. This difference in behavior is likely to produce the "contrast" required for ahead of time detection of approaching boundary.

The simulation of the reflectance ratio also produced an important result (Fig. 5). First, it was observed that at the distance of >1.5 mm from the interface, the ratio remained constant at ~ 0.5 arbitrary units (a.u.). Second, at 1.5 mm from the interface, the ratio started to decrease at an accelerated rate, indicating that the contrast between the wavelengths also increased at an accelerated rate. The maximum rate of change of 1 a.u.mm^{-1} was observed at the distance of 233 μm from the interface. The difference in contrast and its rate of change above and below the 1.5 mm bone layer thickness suggests that in practical measurements, this parameter can be used for detecting the approaching bone-muscle interface, where it would serve as a signal or a trigger. This result indicates that, in a best case scenario, the look ahead distance (LAD) of the drill with 1.3 mm inter-fiber spacing is ~1.5 mm. However, practical experiments had to be carried out to

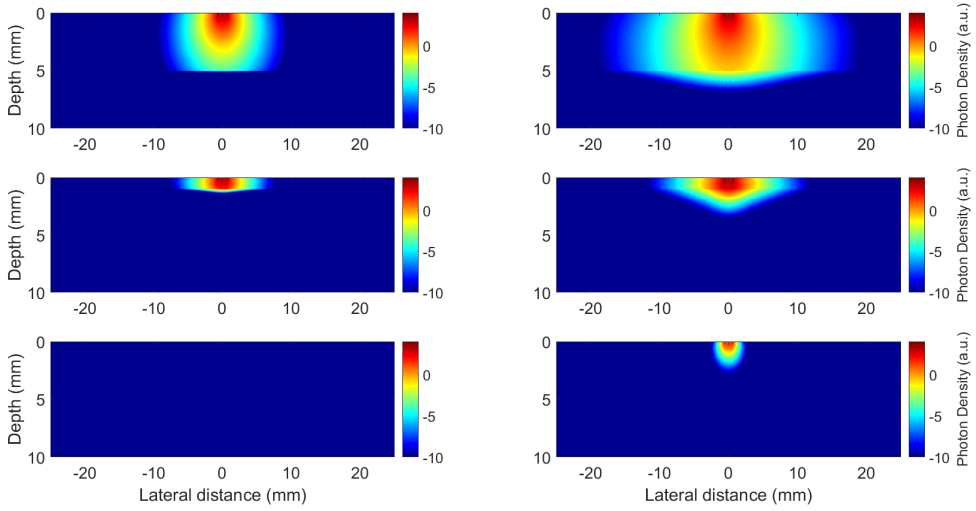

Fig. 4. MC simulation of photon density in bone and muscle layers with source-detector separation of 1.3 mm. Bone thickness shown are 5 mm (Top), 1 mm (Middle) and 0 mm (Bottom). 470 nm is represented on the left, 780 nm is on the right.

Biomedical Optics EXPRESS

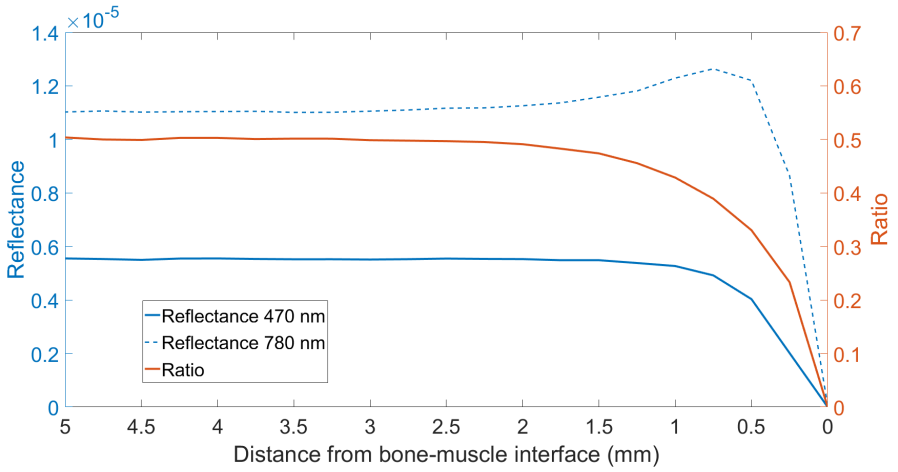

Fig. 5. Simulated reflectance and optical power ratio of 470 nm and 780 nm wavelengths at a range of distances from the bone-muscle interface. Solid blue line, dashed blue line and red line represent 470 nm, 780 nm and ratio of 470/780, respectively.

determine the true LAD of the system.

3.2. LAD measurements using DRS

To determine if two-wavelengths DRS can be used to detect an approaching bone-tissue interface, a series of drill measurements were performed on $n = 4$ bovine femur samples. These experiments were used to identify a particular DRS signal signature associated with the approaching boundary, to estimate the signature period and to calculate the LAD. The measurements were carried out as follows. The bodies of femurs, 15 to 25 cm long, were secured in horizontal orientation on a stage, mounted on top of a load cell, with the attached muscle tissue hanging directly below the bone. Any muscle tissue attached on top of the bone was removed in order to make it easier to position the drill bit. The drill sites were spaced $10mm$ apart, along the body of the femur, in the axial direction. The first set of measurements was performed on $n = 1$ femurs and used a vertical gantry with the drill bit feed rate set to 1 mm sec^{-1} to drill a total of $n = 8$ holes. The second set of experiments was performed on $n = 3$ femurs with the drill held in hand. A total of 42 holes were drilled by hand in the three femur samples. Both sets of experiments measured the load applied to the bone sample and the power of diffusely reflected light at 470 nm and 780 nm in cortical bone, marrow and muscle tissue versus time. The reflectance measurements were then used to calculate optical power ratio between two-wavelengths. As an example, Fig. 6 shows the data from one drilling measurement performed on the gantry, highlighting the effects of sample structures on force and DRS magnitudes.

3.2.1. Gantry-controlled drilling

In the gantry controlled experiment, the approaching boundaries (marrow and muscle) consistently resulted in an observable decrease of optical power ratio followed by the decrease in measured load. The load measurement ranged between 0.8 to 1 a.u. when drilling through bone and decreased to near 0 a.u. when the drill bit entered the marrow or the muscle tissues. The DRS response to the approaching interfaces preceded the measured drop in load as highlighted in Fig. 7. As shown in Fig. 8(a) and( )b, eight bone-muscle interface measurements performed on this femur were noted to have a distinct identifying signature where the optical power ratio decreased

Biomedical Optics EXPRESS

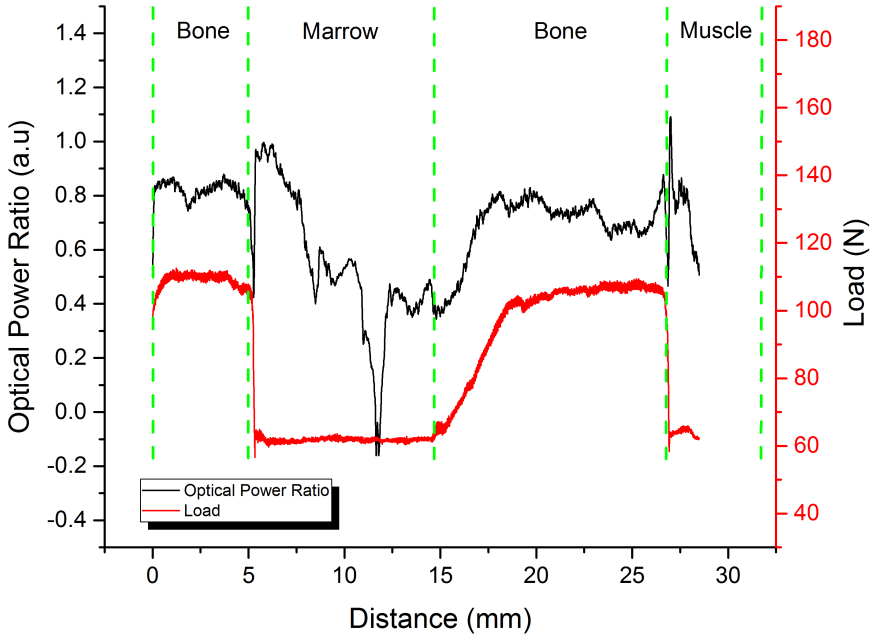

Fig. 6. A single DRS and load measurement versus time when drilling through body of bovine femur at 1 mm sec^{-1}. The transitions between different structures of the sample are highlighted by green, dashed lines.

by ~0.35 a.u. over a period of 250 msec as the drill bit approached the boundary, followed by an increase of ~0.2 a.u.. the following 75 msec. Since the feed rate of the drill during these measurements was 1 mm sec^{-1} and the change of optical ratio occurred over a period of 250 msec, it was possible to determine that in this instance, the LAD was 250 μm and the rate of ratio decrease was 1.4 a.u.mm^{-1}. The measured LAD was six times shorter when compared to the best case scenario, predicted by the MC simulation. However, since the MC showed that the highest rate of change and contrast occurred 233 μm from the interface, the measured LAD of 250 μm indicates that the DRS measurement was only sensitive enough to detect the difference between the wavelengths when 470 nm light underwent near full absorption.

During gantry experiments, prior to the breach event, the optical power ratio showed relatively slow rising and falling trends. Figure 7(a) shows a consistent ratio increase between 2 to 3.5 sec followed by a slow decrease between 3.5 to 5 sec while Fig. 7(b) shows an increase between 21.5 to 22.5 sec followed by a relatively constant ratio value between 22.5 to 24 sec. The load-cell values recorded during the same experiments also show gradual fluctuations, although no obvious correlation with DRS fluctuations could be observed (load plots of Fig. 7(a)and (b). However, the observed changes in load do indicate that the mechanical properties of the bone are changing along the cross-section as previously shown in [33, 34]. Previous reports suggest that the load measurements fluctuations are linked to the variations in the density of the bone material which dictates the mechanical properties of the bone and has a direct effect on μ_s' [9, 35, 36]. However, it is important to point out that in this instance, the DRS measurement by itself, without the

Biomedical Optics EXPRESS

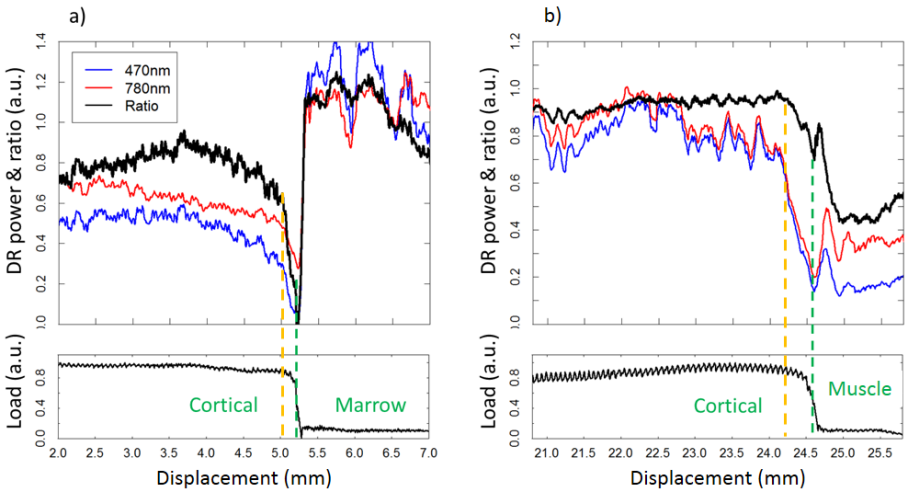

Fig. 7. An example of DRS and load measurements (n = 1) drilled at 1 mm sec^{-1} on a) bone-marrow and b) bone-muscle interfaces of a single femur sample. In both cases, the load measurement drop (green dashed line) lags the drop of the optical power ratio (orange dashed line). This lag in response indicates that the DRS measurement is detecting the approaching bone-tissue interface before the mechanical breach occurs.

complimentary load measurement was not sufficient to distinguish the variation of bone density. The DRS measurements could only be used reliably to differentiate between bone and the approaching muscle tissue.

3.2.2. Hand drilling

Following the gantry controlled experiments, 42 drill measurements were performed on n = 3 bovine femur samples with the drill held in hand. Figure 9 presents the DRS and load data from a single drilling experiment. The measurements for both: bone-marrow and bone-muscle interfaces resembles the data collected during gantry controlled experiments where the optical power ratio decreased before the corresponding load measurement.

From experiments on three samples, 19 out of 42 measurements were used to establish the signature DRS response to the approaching bone-tissue interface and drill bit breakthrough. Figure 10(a) and (b) shows the raw and averaged DRS measurements of bone-muscle interface, respectively. As the drill feed rate was controlled manually and was unknown while the change of DRS was measured against time, there was no capability to determine the LAD directly. In this instance, it was only possible to measure the time period of the ratio change prior to breach. The results showed that the average DRS response signature observed is similar to gantry-controlled experiments where the optical power ratio initially decreased as the drill bit approached the boundary and partially recovered when the breakthrough occurred. The average magnitude of the ratio drop was 0.2 a.u. over a period of 200 msec followed by recovery of 0.05 a.u. over a period of 250 msec. The observed ratio decrease shows that the two-wavelengths DRS measurements are capable of detecting an approaching bone-muscle interface in advance of mechanical breach when drilling by hand. The identified signature has the potential to serve as a trigger for stopping the drill. The following section describes the experiments with automated stopping of the drill triggered by the signature ratio drop.

Biomedical Optics EXPRESS

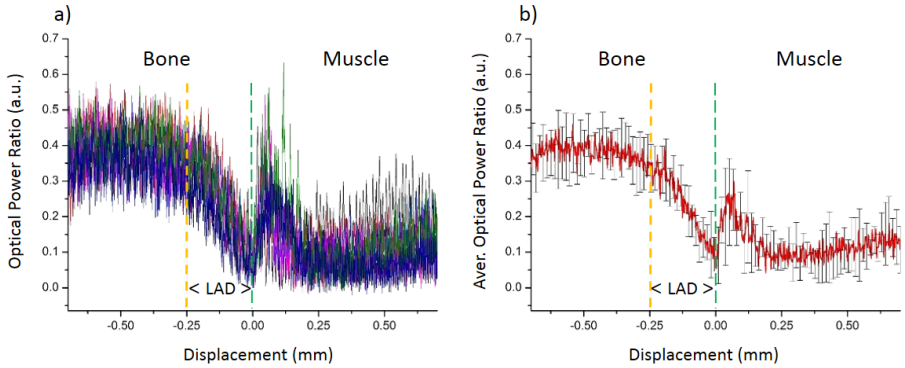

Fig. 8. a) Eight superimposed DRS measurements of bone-tissue interface of single bovine femur sample showing the response of the optical power ratio to the approaching muscle layer. b) The average DRS measurement. Considering drill feed rate was 1 mm sec^{-1}, and the average drop of the optical power ratio occurred over a period of 250 msec, the LAD was calculated to be 250 μm. The LAD is indicated by the distance between the orange and green dashed lines.

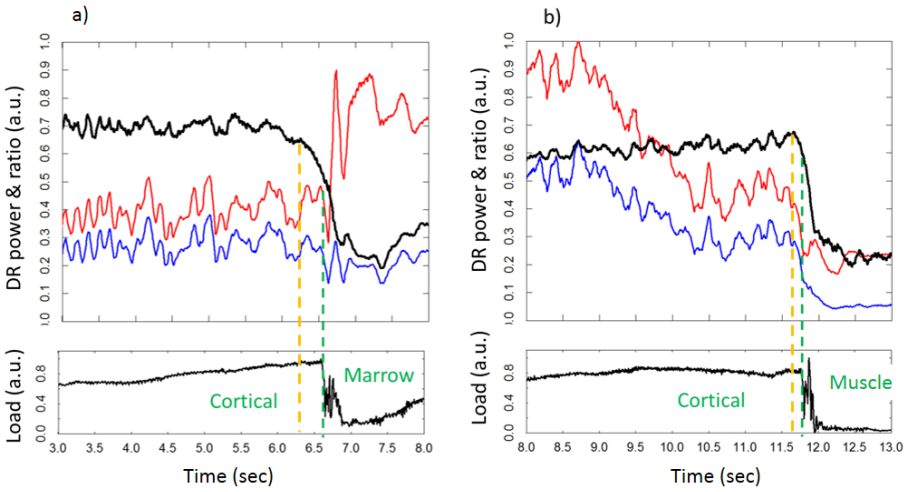

Fig. 9. An example of DRS and load measurements performed on a) bone-marrow and b) bone-muscle interfaces of a single femur sample when drilling by hand. In both cases the load measurement drop (green dashed line) lags the drop of the optical power ratio (orange dashed line).

3.3. *Automated drill-stop before breach*

To determine if the observed, 200 msec long optical ratio signature can be used as an indicator of an approaching tissue boundary and prevent the drill tip cutting into the muscle tissue, a third series of experiments was carried out. For these experiments, $n = 3$ additional femur samples were used and a total of 21 measurements were performed. One femur sample was used to test the drill's stop capability on bone-marrow interface while the remaining two samples were used to test the drill on the bone-muscle interface. Both samples used for bone-muscle interface testing

Biomedical Optics EXPRESS

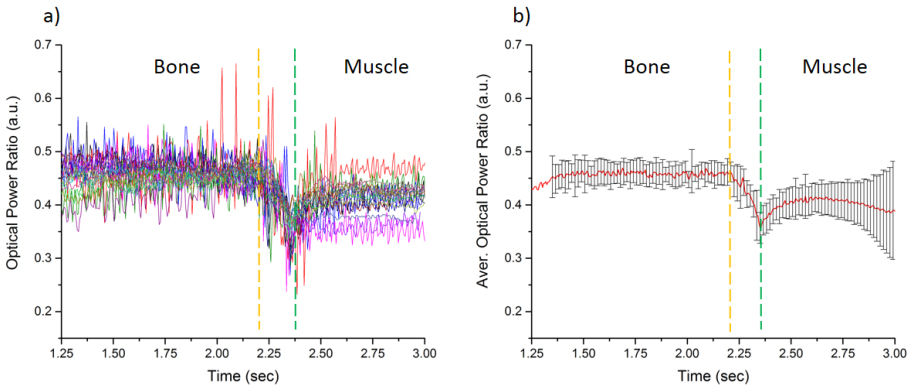

Fig. 10. a) Nineteen superimposed DRS measurements of bone-tissue interface of $n = 3$ bovine femur samples showing the response of the optical power ratio to the approaching muscle layer. b) The average DRS measurement.

were cut in half axially and marrow was removed as it was not required in this instance. These measurements were performed without the use of the load cell, with samples clamped in a vice and drill held in hand.

To automate the stopping of the drill, hardware and software modifications were implemented. First, a relay was integrated into the battery pack of the drill for the purpose of cutting the power to the drill motor. The relay was activated by a 5 V pulse generated by the DAQ as a response to a trigger event. To trigger the relay, a LabView code performed a running linear fit on optical power ratio using a 200 msec window and measured the slope of the fitted line. The slope threshold of -0.35 a.u.sec^{-1} was set as a trigger for relay activation (Fig. 11). These modifications allowed the DRS enhanced drill to continuously monitor the optical power ratio, detect the characteristic ratio changes observed during measurements and disconnect the power from the motor if the slope threshold was reached.

Figure 12(a) shows the cross sections of six holes drilled in the direction of bone-marrow interface using the enhanced drill. Five out of six holes drilled on this sample terminated before the bone-marrow interface was breached, indicating that the slope threshold was reached and the relay was triggered. Holes numbered 2, 4 and 5 show that the drill bit stopped in the range of $\sim$1 mm from the interface and showcase the desired result. The holes numbered 1 and 3 on the other hand show that the drill has stopped much further from the bone-marrow interface at the distance of $\sim$4 to 5 mm. These two drill tests represent a premature condition where the relay was likely triggered by a noise spike (data not shown) rather than the approaching boundary. Figure 12(b)shows the series of holes drilled in the direction of bone-muscle interface. The bones in these experiments were cut in half axially, the marrow was removed and the drill was started from the intramedullary cavity. The muscle tissue was retained during the measurements and was only removed after the measurements were complete to make it easier to expose the profiles of the drilled holes. In 10 out of 15 measurements, the drill automatically stopped in advance of breaching the bone-muscle interface. Specifically, holes numbered 1, 2 and 4 in the top image of Fig. 12(b) and holes numbered $2-7$ in the bottom sample of the same figure also terminated in the range of 1 mm from the interface. The stopping distances observed in these experiments are greater than the LAD of 250 μm observed in Section 3.2.1. As the sample size in this test was too low to account for the inherent variability of biological samples, it is difficult to explain what exactly caused the stop distance discrepancy. A factor that may have influenced the measured distances is that it was difficult to directly measure thickness of the remaining

Biomedical Optics EXPRESS

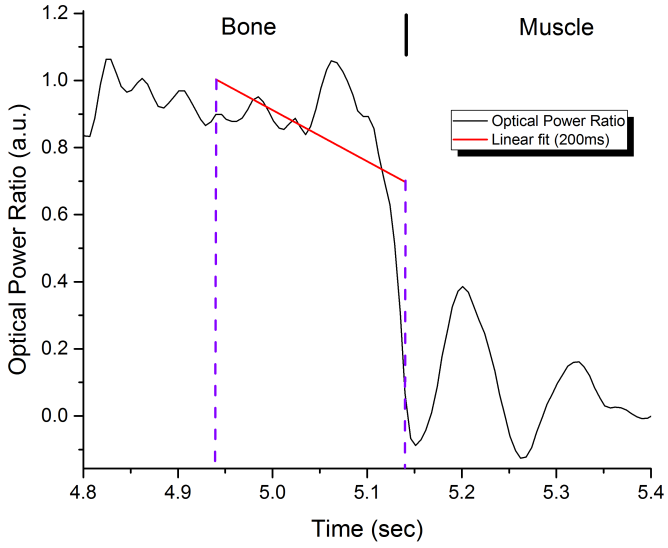

Fig. 11. Graph of linear fit performed on the optical power ratio data when drilling to detect the bone-tissue interface and trigger the drill to stop. Linear fit was performed over a 200 msec period (purple dashed lines) and the slope threshold was set to -0.35 a.u.sec^{-1}.

bone due to i) biological variability of bone surface and ii) the accuracy of the cut to reveal the conical hole profile. Both of these factors have undoubtedly introduced a degree of error into the thickness measurement. Another possible explanation is that the muscle tissue of the femurs used in these tests contained a greater volume of blood as compared to the samples used in the previous experiments. As previously shown, the blood heavily absorbs wavelengths in the blue region compared to NIR [27, 28]. The greater blood concentration possibly absorbed more 470 nm light, increasing the contrast and improving the signature optical ratio response. However, additional experiments, specifically aimed at determining the effects of blood concentration in the muscle need to be carried out to establish the accuracy of the above assessment. In addition to increased stopping distance, the tests also showed that the drill failed to stop in a number of tests, indicating that the slope threshold was not detected, either in time or at all. The likely cause of this is the magnitude of the optical ratio change was insufficient to produce the threshold slope value over the period of 200 msec. Unfortunately, in preliminary tests (data not shown) it was found that decreasing the fitting period or the slope threshold made the drill sensitive to signal noise and produced false positives. Despite stopping distance variation and five drill bit breaches, the tests performed with the automated drill show that the observed signature ratio change in response to the approaching boundary successfully triggered the power cut-off relay and stopped the drill. This is especially evident in the sample shown at the bottom of Fig. 12(b) and indicates that this approach is a strong candidate for future research into smart surgical tools.

Biomedical Optics EXPRESS

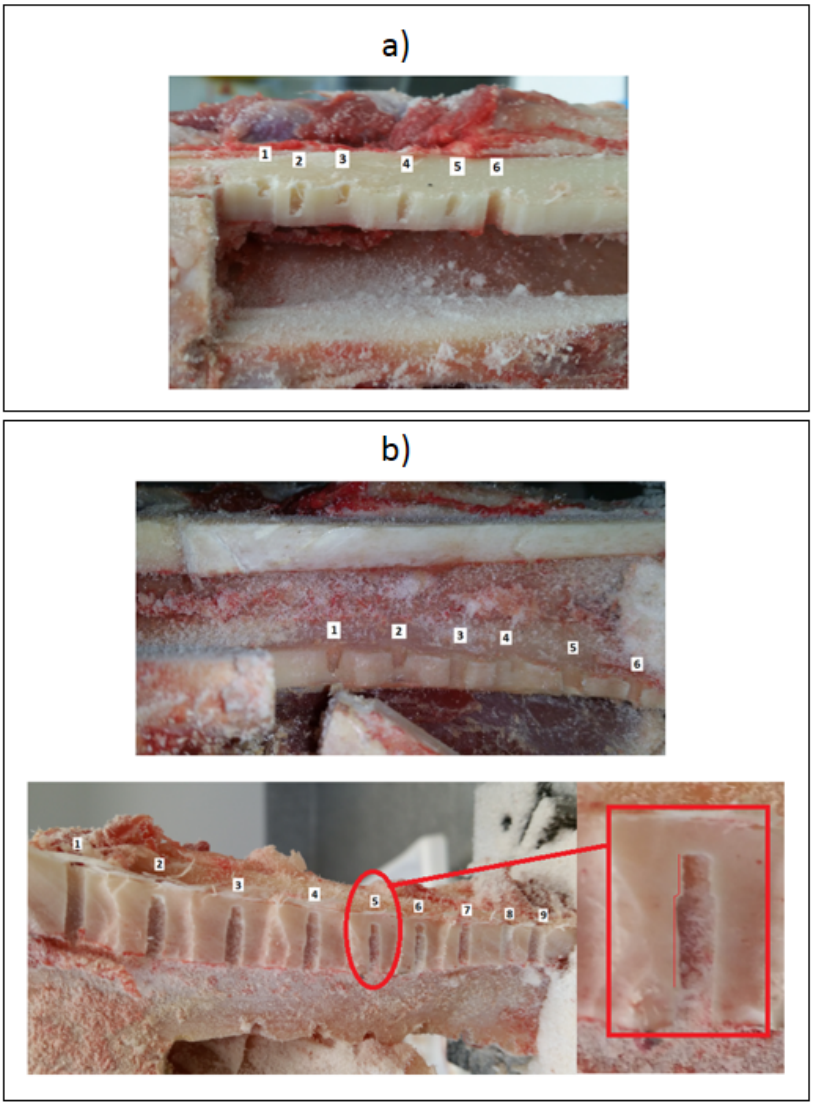

Fig. 12. Image of a bone samples used for a) bone-marrow and b) bone-muscle interface detection. The muscle and marrow tissues have been removed and the cortical bone cut axially to expose the drill hole profiles.

3.4. Limitations and future work

3.4.1. Drill bit integrated POF

The POF integrated into the drill bits were found to be prone to damage and wear at the cutting surface. The damage was primarily caused by abrasion and excessive heat buildup. This limited the lifespan of the drill bit to 10 to 15 measurements (20 to30 individual holes). A more mechanically robust solution, such as integrating a silica "window" at the ends of the fibers or changing the cut relief geometry, is required to extend the drill bit usability.

Biomedical Optics EXPRESS

3.4.2. The PD array

The discontinuity of the PD array was not an optimal solution in terms of signal stability as the sampling was not synchronized with the rotational speed of the drill nor the position of the mirror versus each PD. This introduced a risk that the PD array could be sampled at the exact instant when the mirror-reflected beam was between two adjacent PDs, resulting in loss of signal during that period. However, considering the extreme mechanical constraints of the drill, a commercial instrument manufactured to very high tolerances, the PD array was the best solution to signal acquisition that could be implemented. The optimal PD arrangement would involve coupling a single PD to the collecting fiber of the drill. This would involve integrating photonic as well as electronic capabilities into an assembly rotating at ~ 15000 RPM.

3.4.3. Light coupling

The light path from the LEDs to the tip of the drill bit had to pass through a series of couplers with air-gaps. This resulted in substantial attenuation of the light power delivered to the sample and in turn, it had an effect on the power of diffuse reflectance collected by the detector fiber. In addition, the optical patch cable was built using 500 μm POF. This diameter is relatively small compared to the area of the LED surfaces and incurs losses. A commercial, fiber bundle such as BFY1000LS02 from ThorLabs, UK can be of benefit as it would increase the amount of light delivered to the ball lens at the back end of the drill bit.

4. Conclusion

The research presented in this paper resulted in successful integration of DRS into a functional surgical drill for the purpose of detecting approaching boundaries between bone and muscle. The simulation of the drilling experiments indicated that in the best case scenario, the LAD of the system should be 1.5 mm. In practical, gantry-controlled, measurements, it was observed that the LAD was 250 μm, six times shorter than predicted. However, the MC simulation showed that the optical power ratio rate of change and contrast was largest below 233 μm from the interface. This distance matches more closely to the measured 250 μm LAD and indicates that this DRS system is only sensitive to high contrast between the illuminating wavelengths resulting in lower than predicted LAD. Practical experiments with the automated drill produced encouraging results where the linear fit algorithm was capable of detecting the threshold ratio change of -0.35 a.u.sec^{-1} and cut the power to the drill motor before mechanical breach of the bone. The drill was able to stop ~1 mm from the boundary in eight out of 15 drilling attempts. This paper shows solutions to a number of formidable engineering challenges and the first instance of DRS integration with a dynamic surgical instrument for the purpose of real-time, automated surgical guidance. The outcome of this research highlights the potential of DRS integrated drill to improve outcomes of such orthopedic procedures as IM nailing. The automated boundary detection can help the surgeon to guide the depth of pilot holes for proximal and distal screws thereby avoiding accidental bone tissue boundary breach, soft tissue injury and possible post-operative complications.

Funding

Stryker (Ireland); Science Foundation Ireland (12/RC/2276).

Acknowledgements

The authors of this research would like to acknowledge the contributions of Evans Chikarakara to the LabView code, Noreen Nudds for packaging of photonic components and Kevin Buckley for manuscript reviews. The authors would also like to thank Prof. Stefan Andersson-Engels for sharing his expertise on optical measurements, MC simulations and data processing.

Biomedical Optics EXPRESS

Disclosures

The authors declare that there are no conflicts of interest related to this article.

References

1. S. Nickell, M. Hermann, M. Essenpreis, T. J. Farrell, U. Krämer, and M. S. Patterson, "Anisotropy of light propagation in human skin," Phys. Medicine Biol. **45**, 2873 (2000).
2. U. S. Dinish, C. L. Wong, S. Sriram, W. K. Ong, G. Balasundaram, S. Sugii, and M. Olivo, "Diffuse optical spectroscopy and imaging to detect and quantify adipose tissue browning," Sci. Rep. **7**, 41357 (2017).
3. D. J. Evers, R. Nachabé, H. M. Klomp, J. W. van Sandick, M. W. Wouters, G. W. Lucassen, B. H. Hendriks, J. Wesseling, and T. J. Ruers, "Diffuse reflectance spectroscopy: A new guidance tool for improvement of biopsy procedures in lung malignancies," Clin. Lung Cancer **13**, 424 – 431 (2012).
4. F. Stelzle, A. Zam, W. Adler, K. Tangermann-Gerk, A. Douplik, E. Nkenke, and M. Schmidt, "Optical nerve detection by diffuse reflectance spectroscopy for feedback controlled oral and maxillofacial laser surgery," J. Transl. Medicine **9**, 20 (2011).
5. N. Reistad, J. Nilsson, O. V. Timmermand, C. Sturesson, and S. Andersson-Engels, "Diffuse reflectance spectroscopy of liver tissue," in *SPIE Biophotonics South America,* (International Society for Optics and Photonics, 2015), p. 95314E.
6. C. Brown, C. Jayadev, S. Glyn-Jones, A. Carr, D. Murray, A. Price, and H. Gill, "Characterization of early stage cartilage degradation using diffuse reflectance near infrared spectroscopy," Phys. Medicine Biol. **56**, 2299 (2011).
7. J. S. Soares, I. Barman, N. C. Dingari, Z. Volynskaya, W. Liu, N. Klein, D. Plecha, R. Dasari, and M. Fitzmaurice, "Diagnostic power of diffuse reflectance spectroscopy for targeted detection of breast lesions with microcalcifications," Proc. Natl. Acad. Sci. United States Am. **110**, 471–476 (2013).
8. P. Taroni, D. Comelli, A. Farina, A. Pifferi, and A. Kienle, "Time-resolved diffuse optical spectroscopy of small tissue samples," Opt. Express **15**, 3301–3311 (2007).
9. N. Ugryumova, S. J. Matcher, and D. P. Attenburrow, "Measurement of bone mineral density via light scattering," Phys. Medicine Biol. **49**, 469 (2004).
10. P. R. Bargo, S. A. Prahl, and S. L. Jacques, "Collection efficiency of a single optical fiber in turbid media," Appl. Opt. **42**, 3187–3197 (2003).
11. M. Johns, C. A. Giller, D. C. German, and H. Liu, "Determination of reduced scattering coefficient of biological tissue from a needle-like probe," Opt. Express **13**, 4828–4842 (2005).
12. A. Korff, A. Follmann, T. Fürtjes, T. Jalowy, and K. Radermacher, "Optical sensors for a synergistically controlled osteotomy system," in *Sensors,* (IEEE, 2010), pp. 2069–2072.
13. J. W. Spliethoff, W. Prevoo, M. A. Meier, J. de Jong, H. M. Klomp, D. J. Evers, H. J. Sterenborg, G. W. Lucassen, B. H. Hendriks, and T. J. Ruers, "Real-time in vivo tissue characterization with diffuse reflectance spectroscopy during transthoracic lung biopsy: A clinical feasibility study," Clin. Cancer Res. **22**, 357–365 (2016).
14. V. G. Prabitha, S. Suchetha, J. L. Jayanthi, K. V. Baiju, P. Rema, K. Anuraj, A. Mathews, P. Sebastian, and N. Subhash, "Detection of cervical lesions by multivariate analysis of diffuse reflectance spectra: a clinical study," Lasers Med. Sci. **31**, 67–75 (2016).
15. I. Hacihaliloglu, R. Abugharbieh, A. J. Hodgson, and R. N. Rohling, "Bone surface localization in ultrasound using image phase-based features," Ultrasound Medicine & Biol. **35**, 1475–1487 (2009).
16. J. R. Weber, F. Baribeau, P. Grenier, F. Émond, S. Dubois, F. Duchesne, M. Girard, T. Pope, P. Gallant, O. Mermut *et al.*, "Towards a bimodal proximity sensor for in situ neurovascular bundle detection during dental implant surgery," Biomed. Opt. Express **5**, 16–30 (2014).
17. D. H. Wicaksono, G. Pandraud, E. Margallo-Balbas, P. French, P. Breedveld, and J. Dankelman, "Micro-optics assembly in dental drill as a platform for imaging and sensing during surgical drilling," in *Sensors,* (IEEE, 2010), pp. 265–268.
18. G. Zheng, X. Zhang, D. Haschtmann, P. Gédet, X. Dong, and L.-P. Nolte, "A robust and accurate two-stage approach for automatic recovery of distal locking holes in computer-assisted intramedullary nailing of femoral shaft fractures," IEEE Transactions on Med. Imaging **27**, 171–187 (2008).
19. W. Chu, J. Wang, S.-T. Young, and W. C. Chu, "Reducing radiation exposure in intra-medullary nailing procedures: Intra-medullary endo-transilluminating (imet)," Injury **40**, 1084–1087 (2009).
20. H. Liao, H. Ishihara, H. H. Tran, K. Masamune, I. Sakuma, and T. Dohi, "Precision-guided surgical navigation system using laser guidance and 3d autostereoscopic image overlay," Comput. Med. Imaging Graph. **34**, 46– 4 (2010). Image-Guided Surgical Planning and Therapy.
21. S. Nakdhamabhorn and J. Suthakorn, "A novel surgical navigation concept for closed intramedullary nailing of femur using 4-dof laser-guiding robot," in *Robotics and Biomimetics (ROBIO), 2011 IEEE International Conference on,* (IEEE, 2011), pp. 479–484.
22. M.-S. Lee, S.-Y. Wu, T.-H. Wong, W. Hsu, and T.-K. Chung, "A novel guiding device for distal locking of intramedullary nails," in *Sensors, 2012 IEEE,* (IEEE, 2012), pp. 1–4.
23. J. Choi, J. Kim, J. Y. Hwang, M. Je, J.-Y. Kim, and S.-Y. Kim, "A novel smart navigation system for intramedullary nailing in orthopedic surgery," PloS one **12**, e0174407 (2017).

Biomedical Optics EXPRESS

24. R. Hofstetter, M. Slomczykowski, M. Sati, and L.-P. Nolte, "Fluoroscopy as an imaging means for computer-assisted surgical navigation," Comput. Aided Surg. **4**, 65–76 (1999).
25. K. Gavaghan, T. Oliveira-Santos, M. Peterhans, M. Reyes, H. Kim, S. Anderegg, and S. Weber, "Evaluation of a portable image overlay projector for the visualisation of surgical navigation data: phantom studies," Int. J. Comput. Assist. Eadiology surgery **7**, 547–556 (2012).
26. T. Doke, J. T. Liang, S. Onogi, and Y. Nakajima, "Fluoroscopy-based laser guidance system for linear surgical tool insertion depth control," Int. J. Comput. Assist. Radiol. surgery **10**, 275–283 (2015).
27. W. G. Zijlstra, A. Buursma, and W. P. Meeuwsen-van der Roest, "Absorption spectra of human fetal and adult oxyhemoglobin, de-oxyhemoglobin, carboxyhemoglobin, and methemoglobin." Clin. Chem. **37**, 1633–1638 (1991).
28. P. H. C. Tom Lister, Philip A. Wright, "Optical properties of human skin," J. Biomed. Opt. **17**, 09091 (2012).
29. E. Alerstam, T. Svensson, and S. Andersson-Engels, "Parallel computing with graphics processing units for high-speed monte carlo simulation of photon migration," J. Biomed. Opt. **13**, 060504 (2008).
30. L. Wang, S. L. Jacques, and L. Zheng, "Mcml–monte carlo modeling of light transport in multi-layered tissues," Comput. Methods Programs Biomed. **47**, 131–146 (1995).
31. D. J. Faber, M. C. G. Aalders, E. G. Mik, B. A. Hooper, M. J. C. van Gemert, and T. G. van Leeuwen, "Oxygen saturation-dependent absorption and scattering of blood," Phys. Rev. Lett. **93**, 028102 (2004).
32. V.-D. Tuan, *Biomedical Photonics Handbook* (CRC Press, 2003).
33. C. G. T. R., M. H. D. la Torre-I, J. M. Flores-M., M. D. S. H. M., F. Mendoza-Santoyo, M. de J. Briones-R., and J. Sanchez-P., "Surface structural damage study in cortical bone due to medical drilling," Appl. Opt. **56**, F179–F188 (2017).
34. V. M. Rossi, S. B. Gustafson, and S. L. Jacques, "Characterizing the optical properties of bone using a multi-fiber array and diffuse reflectance spectroscopy," in *Frontiers in Optics 2009/Laser Science XXV/Fall 2009 OSA Optics & Photonics Technical Digest,* (Optical Society of America, 2009), p. FME4.
35. T. Beck, "Measuring the structural strength of bones with dual-energy x-ray absorptiometry: principles, technical limitations, and future possibilities," Osteoporos. Int. **14**, 81–88 (2003).
36. Y. Long, W. D. Leslie, and Y. Luo, "Study of dxa-derived lateral–medial cortical bone thickness in assessing hip fracture risk," Bone Reports **2**, 44–51 (2015).